Aachen Institute for Advanced Study in Computational Engineering Science

Preprint: AICES-2012/09-2

20/September/2012

Characteristics of Testing Conditions for Constitutive Models in Metal Plasticity

M. Bambach, H. M. Bücker, S. Heppner, M. Herty, I. N. Vladimirov

RWTH AACHEN UNIVERSITY

AICES

Financial support from the Deutsche Forschungsgemeinschaft (German Research Foundation) through grant GSC 111 is gratefully acknowledged.

©M. Bambach, H. M. Bücker, S. Heppner, M. Herty, I. N. Vladimirov 2012. All rights reserved

List of AICES technical reports: http://www.aices.rwth-aachen.de/preprints

Characteristics of testing conditions for constitutive models in metal plasticity

M. Bambach* H. M. Bücker† S. Heppner‡ M. Herty§ I. N. Vladimirov¶

September 20, 2012

Abstract

In this work, we propose a method to identify constitutive models and material parameters in engineering applications. The presented method is used in the setting of optimal experimental design. The method is based on successive optimization of a finite set of possible material models. The goal is, for an initially unknown material, to define an optimal test–bed based on a given set of constitutive models and a range of possible parameters. As a result of the algorithm, suitable observation operators and external loads are identified. These are then the optimal experimental conditions under which the parameters of the unknown material are tested.

1 Introduction

The prediction of the behavior of a workpiece during manufacturing or a structure under external loading depends largely on the quality of the constitutive model that is used in the material description. From an abstract point of view, constitutive models (or constitutive equations) link configuration and source variables of a physical theory [37]. For the plastic deformation of metals, for instance, a multitude of constitutive models have been developed to describe the incipient plastic flow, strain hardening and anisotropy, e.g. [41], [22], [7], [12], [42], [31]. When these models are used with solution methods like the finite element method, complex metal forming or deformation processes can be modeled. Unfortunately, Kocks and Mecking [25] give convincing reasons for their rather pessimistic forecast that "an ab initio theory of strain hardening, with a quantitative prediction of the numerical constants, is unlikely to ever be derived even for a specific case, and impossible with any generality". As a consequence, constitutive models for finite strain plastic deformation of metals are not unique and they contain material-dependent constants that have to be determined from experiments. The fact that often a multitude of constitutive models exist which could be used to describe a given material is problematic, since it introduces arbitrariness into

*Institute of Metal Forming, Intzestr. 10, RWTH Aachen University. E-mail: bambach@ibf.rwth-aachen.de
†Institute for Scientific Computing, RWTH Aachen University. E-mail: buecker@sc.rwth-aachen.de
‡Institute of Metal Forming, Intzestr. 10, RWTH Aachen University. E-mail: heppner@ibf.rwth-aachen.de
§Mathematics, Templergraben 55, RWTH Aachen University. E-mail: herty@mathc.rwth-aachen.de
¶Institute of Applied Mechanics, RWTH Aachen University. E-mail: ivaylo.vladimirov@rwth-aachen.de

model predictions. Also, this leads to the question of quantification of the possible error due to a wrong choice of constitutive equations.

To improve the reliability of engineering computations, it seems important to find the most suitable model for a given application. Hence, methods to benchmark different constitutive models are needed, which has to be done based on suitable experiments. The identification of the best-suited constitutive model hence leads to the problem of finding an experimental set-up or test that is best-suited for distinguishing between the constitutive models available. Experimental tests are also the basis for determining the material-dependent parameters entering a constitutive equation. These tests differ, e.g., in the type of loading, geometry, the time history or the measured response of the specimen.

If the model (in our motivating example, the constitutive model) is known, then the problem of identifying parameters in the model has been studied extensively in the literature. For problems with a finite number of parameters, see, e.g., [3, 8], and for problems with distributed parameters see, e.g., [14, 34, 36, 40, 29]. In particular in the case of material laws in elastoplasticity inverse problems have been intensively discussed, e.g., in [28, 19, 26, 21, 20, 2, 35]. Additionally, if one can choose between different material tests, then approaches from optimal experimental designs [3, 32, 38] can be used to select the best material test for parameter identification.

The posed questions are known as model identification problems in the literature. Using approaches from optimal experimental design those questions have been studied in [4, 5, 9, 11, 16, 23, 29]. Many of the existing approaches to model discrimination follow the work of [4]. Therein, discrimination of models using the minimal model distance has been discussed and a measure to identify the best possible model called 'T-optimum' design has been introduced. In the sequential approach of [5], however, it is assumed that the "true" model is already known and available among the set of trial models. The 'T-optimum' design is a function of the distances between all other models and the 'true' model computed using experimental data. If necessary, the guess of the true model is updated based on the new data and the process is repeated. This approach has been followed also in [9, 11, 16, 23, 29] however using different measures on the model distance. For a discussion of the various proposed discrimination criteria we refer to [29]. For example, the model distances proposed in [29] build on the so–called Akaike information criterion (AIC) [1]. The AIC measures the loss of information when the true model is replaced by an approximating model, see also [10]. From the AIC, [29] derive weights for each of the N models under consideration and compute a design by minimizing the sum of the Akaike weights. The Akaike weights, however, depend on current parameter estimates, and statistical information of measurement errors, which are updated based on experiments using the new material tests. As in [5] the result is again a sequential procedure. In each step experimental designs are computed by minimizing the sum of Akaike weights, experiments are conducted, parameter estimates are updated, and the set of candidate models is updated.

In our work, we do not assume that the best or "true" constitutive model is given a priori but has to be determined from experiments as well. We further present a two–step procedure where the fist step is *independent* of any experimental data. While the approaches in [4, 5, 9, 11, 16, 23, 29] sequentially compute material tests and conduct experiments, our new approach requires in the first step a single computation of $N(N-1)/2$ designs to best discriminate between all pairs of models and, in a second stage $N(N-1)$ or, depending on the approach, $N(N-1)/2$ experiments with corresponding data to identify the model.

Unlike existing approaches [5, 9, 11, 16, 23, 29], we additionally provide error bounds on observation and model errors under which the presented approach is guaranteed to determine the correct model. The proposed method is an extension of [6] allowing for observation, measurement errors and errors in the material tests (e.g. deviations in the prescribed external load history from the intended one). This allows for a broad range of applications and in particular allows to include additional information in the model discrimination process. Another novelty of our approach is the use of automatic differentiation to compute the sensitivity of the constitutive models for finite strain plasticity with respect to deviations in the predefined conditions as well as the application to sophisticated realistic constitutive equations for metal forming. Our target application is a family of constitutive models for finite deformation elastoplasticity with isotropic/kinematic hardening. Hence, the experimental design can be computationally expensive. However, if the number of models N is small it is feasible to conduct $N(N-1)$ or, depending on the variant taken, $N(N-1)/2$, experiments. The experiments can be designed in an off-line stage and it is possible to create libraries of experiments.

If the number of models N is large, our approach will likely not be practicable unless experiments can be conducted in a fast and automated way. It is possible that the sequential design approaches terminate in a few steps, and therefore, require relatively few experiments even if the number of models is large. In fact, [29, Sec. 5] show a case study with ten possible models for a simple chemical reaction, where their sequential procedure ends after one iteration.

This paper is organized as follows. The next section describes the mathematical setting of our problem and introduces and analyzes our approach. We focus on the model identification part and give conditions under which the "true" model can be identified. Once the model has been identified, we use standard techniques to identify the parameters in the model. In Section 4 we discuss examples of identifying a model from a family of finite strain plasticity models by means of different external load complexity and illustrate the application of our approach. These examples demonstrate that if the model distances are sufficiently large with respect to observation errors, the true model can be identified.

2 A new method for model identification considering experimental errors

2.1 Direct and inverse problems in finite strain metal plasticity

In the field of finite strain hyperelastic-plasticity, constitutive models consist essentially of an expression for the stress tensor $\boldsymbol{\sigma}$ as a function of the deformation gradient tensor $\mathbf{F}$, a set of material parameters θ and a set of internal variables $\mathbf{Z}_i$, as well as a set of differential equations (so-called evolution equations) for the material time derivatives of the internal variables $\dot{\mathbf{Z}}_i$, i.e.

$$\boldsymbol{\sigma} = f\left(\mathbf{F}, \theta_\sigma, \mathbf{Z}_i\right) \tag{1}$$

$$\dot{\mathbf{Z}}_i = g\left(\mathbf{F}, \theta_Z, \mathbf{Z}_i\right) \tag{2}$$

Usually, the constitutive model is solved within an initial boundary value problem in the context of e.g. the finite element method. The solution of the initial boundary value problem for a given load history is called 'direct' problem. Here, the material parameters, the boundary conditions, and the external

loads are given and as a result, the stress tensor is determined. In this work, the stress computation is performed at the Gauss-point level of a finite element and in a stand-alone manner, based upon a prescribed distribution of the deformation gradient $\mathbf{F}$.

In the case of parameter identification the system response is interchanged with the material parameters. This kind of inverse problem allows for the calculation of optimal material parameters on the basis of given model information, loading and system response.

Inverse problems in parameter identification can be set up on the basis of homogeneous or inhomogeneous tests. Often, e.g. in tensile or compression testing, a constant stress or strain is assumed to exist throughout the specimen. In this case, the solution of the direct problem can be reduced to integrating the constitutive equation for a given strain history for a single point of the specimen which is representative for the entire specimen.

In this case, we can rewrite the constitutive equation in operator form such that a direct relation between the external loads f and the material response y is established, i.e. we write

$$A(\theta)y(t) = f(t), \tag{3}$$

indicating that the operator A represents the result of an integration of the constitutive equation along a given load path $f(t)$. It establishes a mapping

$$A : \Theta \times Y \to \mathcal{F}, \tag{4}$$

where Θ is the set of feasible parameters, Y is the state space and $\mathcal{F}$ is the space of 'external loads'. We assume that all spaces are Banach spaces.

2.2 Approach and conditions for model identification

Suppose we have a system that is described by one out of N parameter-dependent models. We want to identify the "true" model and to that end we can conduct experiments, where for each experiment we prescribe an external load f and record observations Cy of the system state y. We present a method that identifies the true model under measurement errors and errors in the load requiring only few *experiments.*

Our problem is as follows: we have to discriminate between N models and the true model is unknown a priori. We can perform numerical simulations with the different models using a different load f and obtain simulated system states Cy. We assume that the simulation of a system is not as expensive as a true experiment. The simulation of models might therefore be conducted often in contrast to the experiment. When we conduct an experiment then we also assume to have observation errors on the state of the system as well as errors on the system's input. We give conditions under which the presented algorithm correctly identifies the true model. However, in order to state the conditions typically a priori, off-line computations are needed.

Let Θ be the set of admissible parameters, let $\mathcal{F}$ be the set of admissible loads, let Y be the (Banach) space of system states, and let $A_i : \Theta \times Y \to \mathcal{F}$ be the ith model for $i = 1, \ldots, N$. Given a load $f \in \mathcal{F}$, the state y of the ith model with parameter $\theta \in \Theta$ is the solution of

$$A_i(\theta, y) = f. \tag{5}$$

In general the set of admissible parameters, feasible loads, or system states may depend on the model. Typically we cannot observe the entire state, but part of it. Therefore, we introduce the Banach space $\mathcal{Z}$ of observations and a bounded linear observation operator $C : \mathcal{Y} \to \mathcal{Z}$ and assume that our observation of the system state is Cy. In order to obtain a well-posed problem we assume

> For any model $i \in \{1, \dots, N\}$, any loads $f \in \mathcal{F}$, and any system parameter $\theta \in \Theta$, there exists a unique state (solution) $y = y_i(\theta, f) \in \mathcal{Y}$ of (5)
>
> $$A_i(\theta, y) = f.$$
>
> For any model $i \in \{1, \dots, N\}$, any system parameter $\theta \in \Theta$ the solution $y_i(\theta, f)$ is Frechet differentiable and uniformly bounded with respect to f:
>
> $$\max_{f \in \mathcal{F}} \| \frac{\partial}{\partial f} y_i(\theta, f) \|_{L(\mathcal{F}, Y)} \leq c_i(\theta).$$

Suppose that k^* is the index of the true model and that $\theta^*_{k^*}$ is the true parameter. For a load f and an observation operator C, the experiment is

$$z^{\text{obs}} = C y_{k^*}(\theta^*_{k^*}, f + \delta^f) + \delta^o, \tag{6}$$

where δ^f and δ^o represent errors in the load and measurement errors, respectively. Typically, only f, δ^f, δ^o and z^{obs} are known, but neither θ_{k^*} and k^*.

In the following we present a *criterion* to determine the model index k^* from the observations Cy_{k^*} under both load and measurement errors. This process consists of two steps. In the first step, the optimizations problems (7) and (8) have to be computed. This step can be done off-line and might be computationally expensive, however *no* experiments are involved. In a second step, a number of experiments are considered in (10), namely at most $N\ (N-1)$, which allow to identify the model index k^* in an optimal way. We also specify conditions on the measurement and observation errors, permitted during the identification of the model. The precise statement is given in Theorem 2.1 with μ_{ij} as defined in (11).

Given a load $f \in \mathcal{F}$ and an observation operator $C \in \mathcal{C}$, an experiment with model i and parameter θ_i would give the observation $Cy_i(\theta_i, f)$, where $y_i(\theta_i, f)$ solves $A_i(\theta_i, y) = f$, assuming for now no errors. Similarly, an experiment with model j and parameters θ_j would give the observation $Cy_j(\theta_j, f)$. Given $i \neq j$ we determine loads $f_{ij} \in \mathcal{F}$ and an observation operator $C_{ij} \in \mathcal{C}$ by

$$\begin{array}{r} \text{maximize} \\ \text{s.t. } C \in \mathcal{C}, \\ f \in \mathcal{F} \end{array} \left\{ \begin{array}{c} \text{minimize} \qquad \| C \left(y_i(\theta_i, f) - y_j(\theta_j, f) \right) \|_{\mathcal{Z}} \\ \text{s.t. } \theta_i, \theta_j \in \Theta \end{array} \right\}.$$

Let (C_l, f_l), $l = 1, \dots, L$, be all possible combinations of observation operators and inputs and let γ_{ij} be the maximum value

$$\gamma_{ij} = \max_{l=1,\dots,L} \min_{\theta_i \in \Theta, \theta_j \in \Theta} \| C_l \left(y_i(\theta_i, f_l) - y_j(\theta_j, f_l) \right) \|_{\mathcal{Z}}, \tag{7a}$$

$$(C_{ij}, f_{ij}) = \text{argmax}_{l=1,\dots,L} \min_{\theta_i, \theta_j \in \Theta} \| C_l \left(y_i(\theta_i, f_l) - y_j(\theta_j, f_l) \right) \|_{\mathcal{Z}}. \tag{7b}$$

We have $C_{ij} = C_{ji}$, $f_{ij} = f_{ji}$ and $\gamma_{ij} = \gamma_{ji}$. It is important to note here that the optimal value γ_{ij} of (7) is a measure of the distance between the models i and j. Similarly, we compare the observed sensitivity of models i and j by

$$\nu_{ij} = 2 \max_{l=1,\dots,L} \max_{\theta_i \in \Theta, \theta_j \in \Theta} \left\{ \|C_l \frac{\partial}{\partial f} y_i(\theta_i, f_l)\|_{L(\mathcal{F},\mathcal{Z})}, \|C_l \frac{\partial}{\partial f} y_j(\theta_j, f_l)\|_{L(\mathcal{F},\mathcal{Z})} \right\}. \tag{8}$$

Both, (7) and (8) can be solved in an off-line stage. We proceed in the two following steps to determine the true model where we assume that the true model has index k^* and parameter $\theta^*_{k^*}$:

- For $i, j \in \{1, \dots, N\}$ with $i \neq j$

  Conduct an experiment with observation operator C_{ij} and load f_{ij}. This results in an observation

  $$z_{ij}^{\text{obs}} = C_{ij} y_{k^*}(\theta^*_{k^*}, f_{ij} + \delta^f_{ij}) + \delta^o_{ij}, \tag{9}$$

  where $y_{k^*}(\theta^*_{k^*}, f_{ij} + \delta^f_{ij})$ satisfies $A_{k^*}(\theta^*_{k^*}, y) = f_{ij} + \delta^f_{ij}$. Here, δ^f_{ij} are errors in the system's input and δ^o_{ij} are measurement errors.

  Solve the problem

  $$\min_{y \in Y, \theta \in \Theta} \|C_{ij} y - z_{ij}^{\text{obs}}\|_{\mathcal{Z}} \tag{10a}$$

  $$\text{subject to } A_i(\theta, y) = f_{ij} + \delta^f_{ij}, \tag{10b}$$

  and let μ_{ij} denote the value of the objective function of (10) where the minimum is found. That is,

  $$\mu_{ij} = \min_{\theta \in \Theta} \|C_{ij} \hat{y} - z_{ij}^{\text{obs}}\|_{\mathcal{Z}} \tag{11}$$

  where $\hat{y}$ is the solution of (10).

- Let

  $$\nu_{ij} \|\delta^f_{ij}\|_{\mathcal{F}} + \|\delta^o_{ij}\|_{\mathcal{Z}} \leq \tau_{ij}. \tag{12}$$

  Select the model ℓ such that

  $$\mu_{\ell j} \leq \tau_{\ell j},\ j \neq \ell \ \text{ and } \ \mu_{j\ell} \geq \gamma_{j\ell} - \tau_{j\ell},\ j \neq \ell. \tag{13}$$

The next theorem states under which condition the previous method identifies the correct model k^*.

Theorem 2.1 *Let (12) hold true. If*

$$\gamma_{ij} > 2\tau_{ij} \textit{ for all } i = 1, \dots, N \textit{ and all } j = 1, \dots, N, \tag{14}$$

then the true model index k^* is the only index that satisfies (13).

The previous result can be used to classify loads f^* and observation operators C^* as seen in the numerical examples in Section 4.6. The result is an extension of Theorem 1.1 from [6]. Therein, the case of *no errors* in the load has been discussed.

Remark 2.2 *Note that the criterion (13) allows for the following interpretation. In case of sufficiently small errors in observation, measurement and applied load one needs to compare the tables with values $(\gamma_{ij})_{ij}$ and $(\mu_{ij})_{ij}$. The correct model corresponds to a row ℓ with sufficiently small values for $\mu_{\ell,j}$ and to the column of same index ℓ having values larger than $\gamma_{j\ell}$. Under assumption (12) there is only one index ℓ satisfying this condition.*

Proof: Let k^* be the true model index and let $\theta^*_{k^*}$ be the true parameter. Note first that $\gamma_{ij} = \gamma_{ji}$ and that $\nu_{ij} = \nu_{ji}$. For any model $j \neq k^*$ we have $\mu_{k^*j} = \min_{\theta\in\Theta} \|\delta^o_{k^*j}\|_{\mathcal{Z}} \leq \tau_{k^*j}$. For any two models $i \neq j$, $\theta, \tilde\theta \in \Theta$ and for all $f \in \mathcal{F}, C \in \mathcal{C}$ we have

$$\begin{aligned}
\|C\left(y_i(\theta, f+\delta^f) - y_j(\tilde\theta, f+\delta^f)\right) - \delta^o\|_{\mathcal{Z}} \leq \\
\|C\left(y_i(\theta, f) - y_j(\tilde\theta, f)\right)\|_{\mathcal{Z}} + \|\delta^o\|_{\mathcal{Z}} + \\
\|C\left(y_i(\theta, f+\delta^f) - y_i(\theta, f)\right) - C\left(y_j(\tilde\theta, f+\delta^f) - y_j(\tilde\theta, f)\right)\|_{\mathcal{Z}} \leq \\
\|C\left(y_i(\theta, f) - y_j(\tilde\theta, f)\right)\|_{\mathcal{Z}} + \|\delta^o\|_{\mathcal{Z}} + \\
\|\delta^f\|_{\mathcal{F}} \left(\max_{\tilde f\in\mathcal{F}} \left\{\|C\frac{\partial}{\partial f} y_i(\theta, \tilde f)\|_{L(\mathcal{F},\mathcal{Z})}\right\} + \max_{\tilde f\in\mathcal{F}} \left\{\|C\frac{\partial}{\partial f} y_j(\tilde\theta, \tilde f)\|_{L(\mathcal{F},\mathcal{Z})}\right\}\right) \leq \\
\|C\left(y_i(\theta, f) - y_j(\tilde\theta, f)\right)\|_{\mathcal{Z}} + \|\delta^o\|_{\mathcal{Z}} + \\
\|\delta^f\|_{\mathcal{F}}\ 2\ \max_{\tilde f\in\mathcal{F}} \left\{\|C\frac{\partial}{\partial f} y_i(\theta, \tilde f)\|_{L(\mathcal{F},\mathcal{Z})}, \|C\frac{\partial}{\partial f} y_j(\tilde\theta, \tilde f)\|_{L(\mathcal{F},\mathcal{Z})}\right\}.
\end{aligned}$$

Hence,

$$\begin{aligned}
\gamma_{jk^*} \leq \min_{\theta\in\Theta} \|C_{jk^*}\left(y_j(\theta, f_{jk^*}) - y_{k^*}(\theta^*_{k^*}, f_{jk^*})\right)\|_{\mathcal{Z}} \leq \\
\min_{\theta\in\Theta} \|C_{jk^*}\left(y_j(\theta, f_{jk^*} + \delta^f_{jk^*}) - y_{k^*}(\theta^*_{k^*}, f_{jk^*} + \delta^f_{jk^*})\right) - \delta^o_{jk^*}\|_{\mathcal{Z}} + \|\delta^o_{jk^*}\|_{\mathcal{Z}} + \\
2\|\delta^f_{jk^*}\|_{\mathcal{F}} \min_{\theta\in\Theta} \max_{\tilde f\in\mathcal{F}} \left\{\|C_{jk^*}\frac{\partial}{\partial f} y_i(\theta, \tilde f)\|_{L(\mathcal{F},\mathcal{Z})}, \|C_{jk^*}\frac{\partial}{\partial f} y_{k^*}(\theta^*_{k^*}, \tilde f)\|_{L(\mathcal{F},\mathcal{Z})}\right\} \leq \\
\mu_{jk^*} + \|\delta^o_{jk^*}\|_{\mathcal{Z}} + \\
2\|\delta^f_{jk^*}\|_{\mathcal{F}} \max_{\theta\in\Theta} \max_{\tilde f\in\mathcal{F}} \left\{\|C_{jk^*}\frac{\partial}{\partial f} y_i(\theta, \tilde f)\|_{L(\mathcal{F},\mathcal{Z})}, \|C_{jk^*}\frac{\partial}{\partial f} y_{k^*}(\theta^*_{k^*}, \tilde f)\|_{L(\mathcal{F},\mathcal{Z})}\right\} \leq \\
\mu_{jk^*} + \|\delta^o_{jk^*}\|_{\mathcal{Z}} + \|\delta^f_{jk^*}\|_{\mathcal{F}}\nu_{jk^*} \leq \mu_{jk^*} + \tau_{jk^*},
\end{aligned}$$

and the true model satisfies (13). Assume (14) holds true and let $\ell \neq k^*$. From the previous computations we have

$$\gamma_{\ell k^*} \leq \mu_{\ell k^*} + \tau_{\ell k^*}$$

and therefore due to (13)

$$\gamma_{\ell k^*} \leq 2\tau_{\ell k^*}$$

which violates (14). Hence, k^* is the only index satisfying (13). □

3 Practical implementation of the algorithm

From an implementation point of view, the algorithm introduced in the previous section essentially consists of a sequence of different minimization problems, the solutions of which are then combined to identify the model. Since we are interested in a local solution of these minimization problems, we employ derivative-based techniques that rely on accurate evaluations of derivatives. A derivative-based algorithm for the solution of a minimization problem

$$\min_x h(x)$$

repeatedly evaluates not only the smooth objective function h at a point x_0 but also its derivative $\partial h/\partial x$ at the same point of interest x_0. This class of methods is described in various textbooks [17, 13, 15, 30, 24]. In this section, the focus is on the different types of minimization problems and the evaluation of the underlying derivatives.

The building blocks of the novel model identification algorithm introduced in the previous section are given by three different types of minimization problems. The first minimization problem is involved in (7a) and is of the form

$$\min_{\theta_i,\theta_j\in\Theta} \|C_l \left(y_i(\theta_i, f_l) - y_j(\theta_j, f_l)\right) \|_{\mathcal{Z}} \tag{15}$$

for some fixed index l. Here, the evaluation of the objective function requires the evaluation of the model $y_i(\theta_i, f_l)$ solving $A_i(\theta_i, y) = f_l$ for a given model index i, material parameter $\theta_i \in \Theta$, and load $f_l \in \mathcal{F}$. Similarly, it is necessary to evaluate the derivative of the system state with respect to the material parameter, $\partial y_i/\partial\theta$, at some parameter θ_i. From the solutions of various instances of this optimization problem we finally arrive at γ_{ij}.

The second type of optimization problem is involved in (8) and consists of

$$\max_{\theta_i\in\Theta} \|C_l \frac{\partial}{\partial f} y_i(\theta_i, f_l)\|_{L(\mathcal{F},\mathcal{Z})}$$

for a fixed index l. Here, the evaluation of the objective function requires the evaluation of the derivative of the system state with respect to the load, $\partial y_i/\partial f$, at some load f_l. It is also necessary to evaluate the second-order derivatives $\partial^2 y_i/(\partial f\,\partial\theta)$ at the input f_l and parameter θ_i. With solutions of these kinds of optimization problems we then compute ν_{ij}.

The third type arises from (10) and is given by

$$\min_{\theta_{ij}\in\Theta} \|C_{ij} y(\theta_{ij}, f_{ij} + \delta_{ij}^f) - z_{ij}^{\text{obs}}\|_{\mathcal{Z}}.$$

Similarly to the first minimization problem, it is once more necessary to evaluate the model y_i and its derivative $\partial y_i/\partial\theta$ at some parameter θ_{ij}. This eventually leads to μ_{ij}.

From a computational point of view, given a program for the evaluation of the model $y(\theta, f)$, a derivative-based algorithm for the solution of the new model identification approach will require the evaluation of the model y as well as its derivatives

$$\frac{\partial y}{\partial\theta}, \quad \frac{\partial y}{\partial f}, \quad \frac{\partial^2 y}{\partial f\,\partial\theta}. \tag{16}$$

A set of techniques commonly referred to as automatic differentiation is capable of transforming the given program for the computation of the constitutive model y into new programs for the computation of the derivatives (16). In general, it is difficult and error-prone to derive and implement analytic formulae for these derivatives by hand. This is the reason why they are traditionally approximated by divided differences. The implementation effort of this numerical differentiation is low since it only requires the repeated evaluation of the model at suitably perturbed input arguments. However, it always involves a truncation error, caused by cutting off the Taylor series. Automatic differentiation, in contrast, does not involve any truncation error and, thus, helps to avoid potential numerical instabilities. An introduction to these techniques is given in [33, 18].

4 Application to finite strain hyperelastic-plasticity

In this section we apply the model identification method proposed in Section 2 to a framework of finite strain hyperelastic-plasticity with isotropic and kinematic hardening to illustrate the capabilities of the novel approach.

4.1 A constitutive framework for finite strain plasticity with isotropic and kinematic hardening

Constitutive models for finite deformation plasticity are widely used for the description of plastic yielding and hardening of metallic materials. The model framework considered in this work consists essentially of three different approaches of describing the hardening behavior in metals. Based on this common framework constitutive models for (1) isotropic, (2) kinematic, and (3) combined hardening can be formulated. These models are to be utilized later in the model identification step of the optimization algorithm.

In this research, the stress computation is done at the Gauss-point level of a finite element in a stand-alone manner, based upon a prescribed distribution of the deformation gradient $\mathbf{F}$. The latter is the fundamental kinematic quantity in the regime of finite strains and can be used for the calculation of the true (or logarithmic) strain tensor $ln\mathbf{V}$. Note that $\mathbf{F}$ plays the role of the external load f in Eq. (3) and serves as input data for the constitutive model. Typically, a distribution $\mathbf{F}(t)$, characterizing the homogeneous experimental test, is input into the constitutive model. The latter computes the true stress tensor $\boldsymbol{\sigma}(t)$, which corresponds to the material response y in Eq. (3), i.e.

- input (external load): $f(t) \leftrightarrow \mathbf{F}(t)$
- output (material response): $y(t) \leftrightarrow \boldsymbol{\sigma}(t)$

A thorough derivation of the constitutive equations in a thermodynamically consistent setting is presented in the work [39]. For clarity, the most important steps of the derivation are summarized here. The starting point is the classical multiplicative decomposition of the deformation gradient $\mathbf{F} = \mathbf{F}_e\,\mathbf{F}_p$ into elastic ($\mathbf{F}_e$) and plastic ($\mathbf{F}_p$) parts. In order to model nonlinear kinematic hardening the additional multiplicative split of the plastic part of the deformation gradient into elastic and inelastic parts is introduced, i.e.

$\mathbf{F}_p = \mathbf{F}_{p_e}\,\mathbf{F}_{p_i}$. In this way, a continuum mechanical extension of the rheological model of Armstrong–Frederick kinematic hardening can be attained. According to [27], this additional multiplicative split can be physically motivated by interpreting the elastic part of the plastic deformation gradient $\mathbf{F}_{p_e}$ as resulting from dislocation-induced lattice rotations on the microscale, whereas $\mathbf{F}_{p_i}$ relates to local plastic deformations.

The Helmholtz free energy per unit volume is assumed to have the form

$$\psi = \psi_e\left(\mathbf{C}_e\right) + \psi_{kin}\left(\mathbf{C}_{p_e}\right) + \psi_{iso}\left(\kappa\right) \tag{17}$$

where $\mathbf{C}_e = \mathbf{F}_e^T\,\mathbf{F}_e = \mathbf{F}_p^{-T}\,\mathbf{C}\,\mathbf{F}_p^{-1}$ is the elastic right Cauchy–Green deformation tensor and $\mathbf{C}_{p_e} = \mathbf{F}_{p_e}^T\,\mathbf{F}_{p_e} = \mathbf{F}_{p_i}^{-T}\,\mathbf{C}_p\,\mathbf{F}_{p_i}^{-1}$ the elastic part of the plastic right Cauchy–Green tensor $\mathbf{C}_p$. Herein, $\mathbf{C} = \mathbf{F}^T\,\mathbf{F}$ designates the right Cauchy–Green deformation tensor. The first part ψ_e represents the macroscopic elastic material properties. The second term ψ_{kin} corresponds to the elastic energy stored in dislocation fields due to kinematic hardening. The third term ψ_{iso} describes the additional amount of stored energy due to isotropic hardening where κ is the accumulated plastic strain.

Utilizing the Clausius–Duhem form of the second law of thermodynamics $-\dot{\psi} + \mathbf{S}\cdot\frac{1}{2}\,\dot{\mathbf{C}} \geq 0$ and assuming that the Helmholtz free energy ψ is an isotropic function of its arguments $\mathbf{C}_e$ and $\mathbf{C}_{p_e}$, one obtains a relation for the second Piola–Kirchhoff stress tensor

$$\mathbf{S} = 2\,\mathbf{F}_p^{-1}\,\frac{\partial\psi_e}{\partial\mathbf{C}_e}\,\mathbf{F}_p^{-T} \tag{18}$$

and evolution equations for the plastic deformation

$$\mathbf{d}_p = \dot{\lambda}\,\frac{\partial\Phi}{\partial\mathbf{M}} = \dot{\lambda}\,\frac{\mathbf{M}^D - \boldsymbol{\chi}^D}{||\mathbf{M}^D - \boldsymbol{\chi}^D||} \tag{19}$$

as well as for kinematic and isotropic hardening, respectively:

$$\mathbf{d}_{p_i} = \dot{\lambda}\,\frac{b}{c}\,\mathbf{M}_{kin}^D\,, \quad \dot{\kappa} = \sqrt{\frac{2}{3}}\,\dot{\lambda} \tag{20}$$

Here, $\mathbf{d}_p$ is the symmetric part of the plastic velocity gradient $\mathbf{l}_p = \dot{\mathbf{F}}_p\,\mathbf{F}_p^{-1}$. Analogously, $\mathbf{d}_{p_i}$ denotes the symmetric part of $\mathbf{l}_{p_i} := \dot{\mathbf{F}}_{p_i}\,\mathbf{F}_{p_i}^{-1}$. The yield function Φ is of von Mises type and reads

$$\Phi = ||\mathbf{M}^D - \boldsymbol{\chi}^D|| - \sqrt{\frac{2}{3}}\,(\sigma_y - R) \tag{21}$$

where $R = -\partial\psi_{iso}/\partial\kappa$ is the isotropic hardening stress-like variable and the superscript D denotes the deviator, i.e. $\mathbf{A}^D = \mathbf{A} - \frac{1}{3}\,(\mathrm{tr}\,\mathbf{A})\,\mathbf{1}$. The quantities $\mathbf{M} = 2\,\mathbf{C}_e\,(\partial\psi_e/\partial\mathbf{C}_e)$ and $\mathbf{M}_{kin} = 2\,\mathbf{C}_{p_e}\,(\partial\psi_{kin}/\partial\mathbf{C}_{p_e})$ represent symmetric Mandel-type stress tensors. The tensor $\boldsymbol{\chi} := 2\,\mathbf{F}_{p_e}\,(\partial\psi_{kin}/\partial\mathbf{C}_{p_e})\,\mathbf{F}_{p_e}^T$ is the back stress in the intermediate configuration and $\dot{\lambda}$ is the plastic multiplier. A dot between two second-order tensors describes their scalar product. Finally, the Kuhn–Tucker conditions $\dot{\lambda} \geq 0$, $\Phi \leq 0$, $\dot{\lambda}\,\Phi = 0$ complete the set of constitutive equations.

The numerical implementation of the constitutive equations is suitably performed in the undeformed or reference configuration. Carrying out the corresponding pull-back of the tensors $\mathbf{M}$, $\mathbf{M}_{kin}$ and $\boldsymbol{\chi}$ and utilizing the relation $\dot{\mathbf{C}}_p = 2\,\mathbf{F}_p^T\,\mathbf{d}_p\,\mathbf{F}_p$ enables the representation of the constitutive equations in the reference configuration:

Table 1: Material parameters

μ	shear modulus [MPa]
Λ	Lamé constant [MPa]
σ_y	initial yield stress [MPa]
b	rate of change of kinematic hardening modulus [-]
c	initial kinematic hardening modulus [MPa]
β	rate of change of elastic range size [-]
Q	maximum change in size of elastic range [MPa]

- Second Piola-Kirchhoff stress $\mathbf{S}$, back stress $\mathbf{X}$ and effective stress tensors $\mathbf{Y}$, $\mathbf{Y}_{kin}$

$$\mathbf{S} = 2\mathbf{F}_p^{-1}\frac{\partial \psi_e}{\partial \mathbf{C}_e}\mathbf{F}_p^{-T},\ \mathbf{X} = 2\mathbf{F}_{p_i}^{-1}\frac{\partial \psi_{kin}}{\partial \mathbf{C}_{p_e}}\mathbf{F}_{p_i}^{-T},\ \mathbf{Y} = \mathbf{C}\mathbf{S} - \mathbf{C}_p\mathbf{X} = \mathbf{C}\mathbf{S} - \mathbf{Y}_{kin} \tag{22}$$

- Plastic flow rule

$$\dot{\mathbf{C}}_p = 2\,\dot{\lambda}\,\frac{\mathbf{Y}^D\,\mathbf{C}_p}{\sqrt{\mathbf{Y}^D\cdot(\mathbf{Y}^D)^T}} \tag{23}$$

- Evolution equation for kinematic hardening

$$\dot{\mathbf{C}}_{p_i} = 2\,\dot{\lambda}\,\frac{b}{c}\,\mathbf{Y}_{kin}^D\,\mathbf{C}_{p_i} \tag{24}$$

- Evolution equation for isotropic hardening

$$\dot{\kappa} = \sqrt{\frac{2}{3}}\,\dot{\lambda} \tag{25}$$

- Yield function

$$\Phi = \sqrt{\mathbf{Y}^D\cdot(\mathbf{Y}^D)^T} - \sqrt{\frac{2}{3}}\,(\sigma_y + Q\,(1 - e^{-\beta\,\kappa})) \tag{26}$$

- Kuhn–Tucker conditions

$$\dot{\lambda} \geq 0, \quad \Phi \leq 0, \quad \dot{\lambda}\,\Phi = 0 \tag{27}$$

Here, $\mathbf{X}$ is the back stress tensor in the reference configuration, $\mathbf{Y}$ and $\mathbf{Y}_{kin}$ are effective stress-like quantities, resulting from the pull-back of the Mandel-type stress tensors.

The internal variables of the model $\mathbf{Z}_i, i = 1,2,3$ are $\mathbf{C}_p = \mathbf{F}_p^T\,\mathbf{F}_p$, $\mathbf{C}_{p_i} = \mathbf{F}_{p_i}^T\,\mathbf{F}_{p_i}$ and κ which describe the evolution of plastic deformation, the evolution of kinematic hardening, and the evolution of isotropic hardening, respectively. The true (or Cauchy) stress tensor is computed by the push-forward of the second Piola–Kirchhoff stress tensor into the current configuration

$$\boldsymbol{\sigma} = \frac{1}{\mathrm{det}\mathbf{F}}\,\mathbf{F}\,\mathbf{S}\,\mathbf{F}^T \tag{28}$$

The framework of constitutive equations includes a total number of 7 material parameters (see Table 1).

4.2 Individual models and loads

The constitutive framework summarized in Section 4.1 can be interpreted as a set of three hardening models for finite plastic deformation that can be switched on or off depending on the values of the material parameters:

- **Model 1** (pure isotropic hardening) is selected by setting the values of the kinematic hardening parameters equal to zero, i.e. $b = 0$ and $c \approx 0$ (to avoid numerical difficulties). This corresponds to $A_1(\theta, y) = f$ with f describing the distribution of the deformation gradient $\mathbf{F}$ and y being the computed stress $\boldsymbol{\sigma}$.
- **Model 2** (pure kinematic hardening) is active when the isotropic hardening parameters β and Q are set equal to zero ($\beta = 0$, $Q = 0$).
- **Model 3** (combined hardening) includes both hardening types and represents the complete framework of finite strain plasticity with combined hardening.

In this way, the three approaches to model the hardening behavior of metals can be used in the optimization method for identifying optimal tests and constitutive models. Due to the fact that the elasticity constants μ and Λ and the initial yield stress σ_y are known in advance and have no influence on the hardening behavior, only the hardening parameters b, c, β and Q have to be varied in the optimization. Thus, the array of material parameters θ reads:

$$\theta = (b, c, \beta, Q) \tag{29}$$

It should be noted that Model 1 (Q, β) and Model 2 (b, c) are each characterized by two parameters to be optimized, whereas the parameter identification of Model 3 consists of all 4 hardening parameters.

In addition, we define a set of five different external loads that impose different time-dependent distributions of $\mathbf{F}$. For this purpose, a strain-controlled simple shear loading is considered here, which means that the distribution of the shear component F_{12} is prescribed as input. The course of the loading magnitude for the five cases is shown in Figure 1. The three normal components of $\mathbf{F}$ have the value 1.0 during the whole simulation, whereas the remaining shear components are set equal to 0.0.

4.3 Comparison of model behavior for different loads

4.3.1 Model 1 vs. Model 2

In the following, the maximal and minimal distances between the models, as identified by the optimization algorithm, are depicted by means of time distributions of the computed stress component σ_{12} during the simple shear loading. The calculated $\sigma_{12} - t$ curves are shown for each of the five considered external loads. Figures 2 to 6 illustrate the greatest distance between Models 1 and 2 for loads 1 to 5. Herein, the blue curves correspond to Model 1 whereas the red ones characterize Model 2. Obviously, the optimization algorithm has identified isotropic (for Model 1) and kinematic (for Model 2) hardening parameters

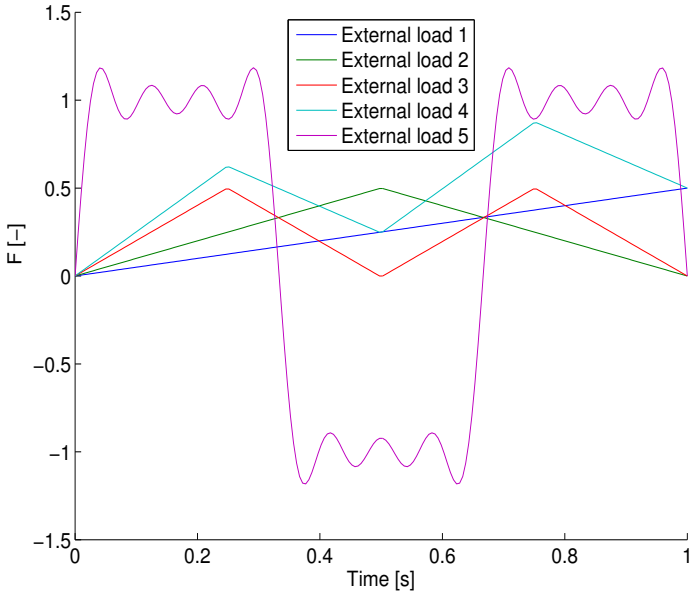

Figure 1: Loading magnitude

which result in significant differences between the computed stress response. For the identified parameters Model 1 predicts strong hardening and relatively late saturation whereas Model 2 is characterized by weak hardening and fast saturation.

The minimal distances between Model 1 and Model 2 for the 5 loads are shown in Figures 7 to 11. Not surprisingly, the monotonic loading (load 1) is not suitable to distinguish between the two hardening models (Figure 7). Both models are capable of predicting an identical hardening response, minimizing the distance between them. The loading-unloading case (load 2, Figure 8) is, on the other hand, capable of distinguishing between Model 1 and Model 2, since the minimal distance is non-negative and no identical stress response can be obtained. It is interesting to note that the optimal result for the minimal distance is characterized by different stress responses both for tensile and compressive stresses (Figure 8), although the two models are capable of predicting the same tensile response (Figure 7).

4.3.2 Model 1 vs. Model 3

The maximal distance between the isotropic (Model 1) and the combined (Model 3) hardening models is depicted in Figures 12 to 16. Herein, the results of Model 1 are represented by blue curves whereas the red curves correspond to Model 3. Since the material response of Model 3 is generally intermediate of the results obtained by Model 1 and Model 2, the maximal distance for monotonic loading in Figure 12 is smaller than the distance between Models 1 and 2 (Figure 2). Quite interesting is the optimal result for load 4 (Figure 15). Clearly, the algorithm has identified the hardening parameters in such a way, that the result of Model 3 is described by very steep hardening behavior and no saturation at all.

The results for the minimal distance between Model 1 and Model 3 are shown in Figures 17 to 21. Again, load 1 (Figure 17) is not suitable to differentiate between the models. The minimal distance for load 2 (Figure 18) is, however, smaller than the corresponding result in Figure 8. Obviously, in this case the

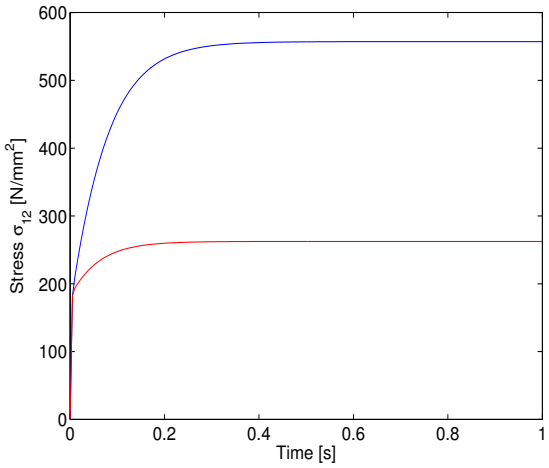

Figure 2: Maximal distance: Model 1 vs. Model 2, load 1

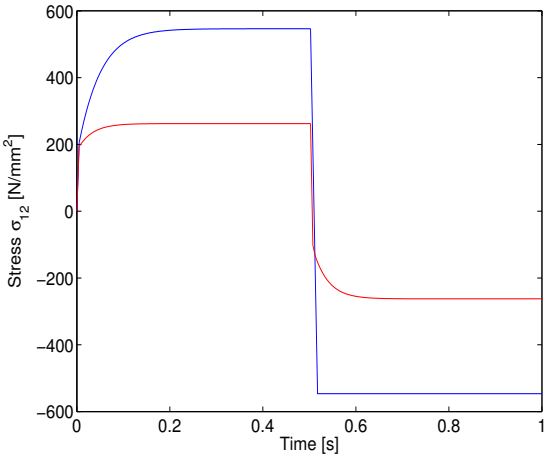

Figure 3: Maximal distance: Model 1 vs. Model 2, load 2

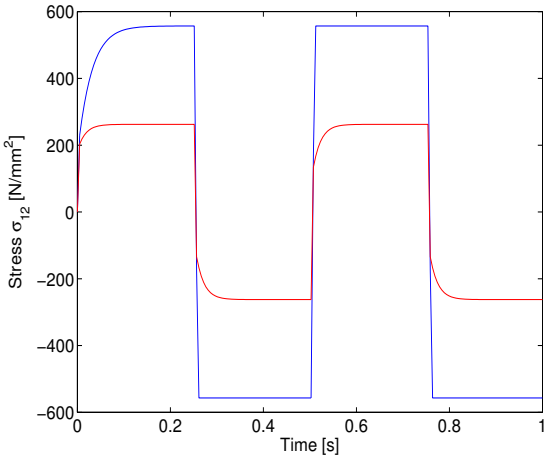

Figure 4: Maximal distance: Model 1 vs. Model 2, load 3

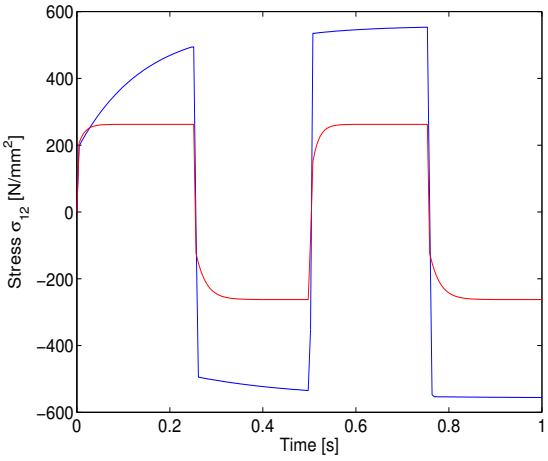

Figure 5: Maximal distance: Model 1 vs. Model 2, load 4

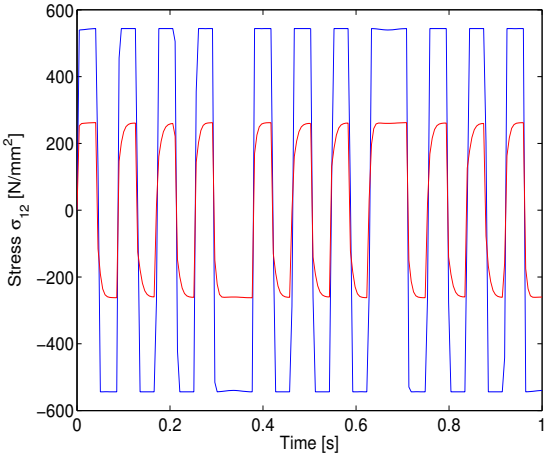

Figure 6: Maximal distance: Model 1 vs. Model 2, load 5

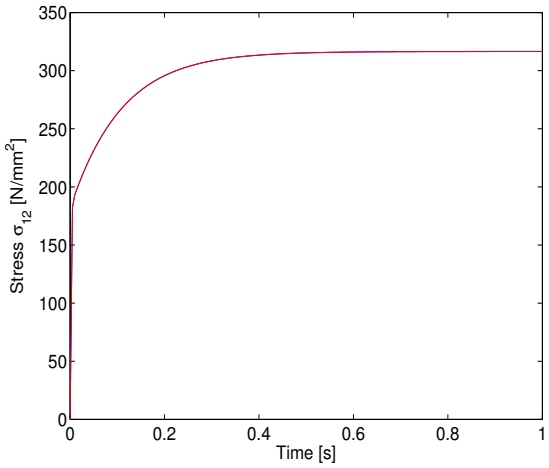

Figure 7: Minimal distance: Model 1 vs. Model 2, load 1

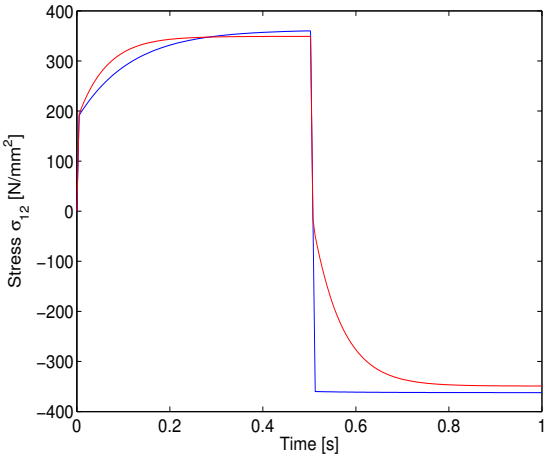

Figure 8: Minimal distance: Model 1 vs. Model 2, load 2

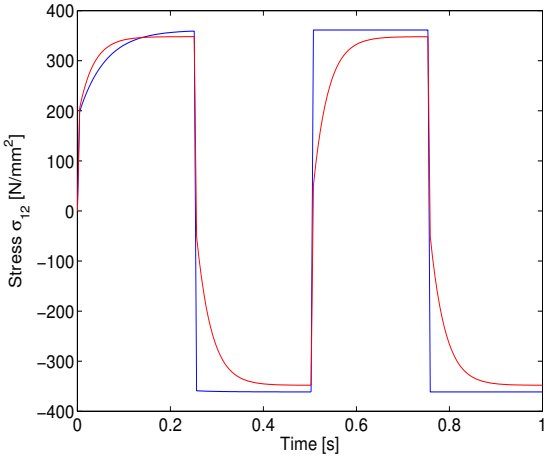

Figure 9: Minimal distance: Model 1 vs. Model 2, load 3

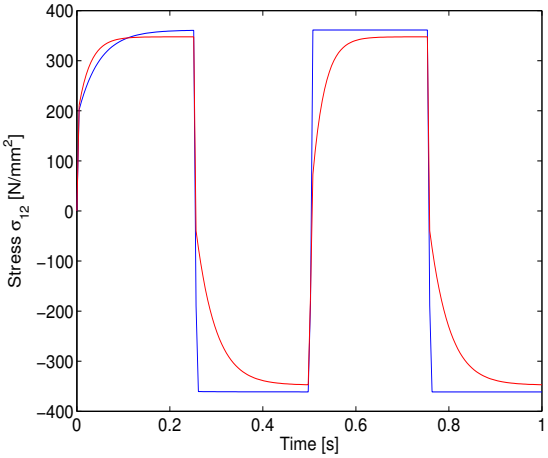

Figure 10: Minimal distance: Model 1 vs. Model 2, load 4

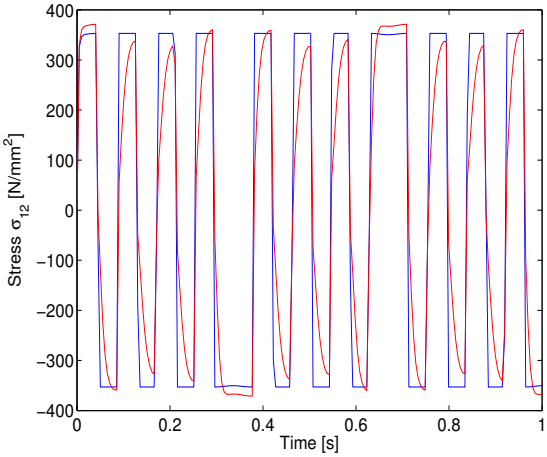

Figure 11: Minimal distance: Model 1 vs. Model 2, load 5

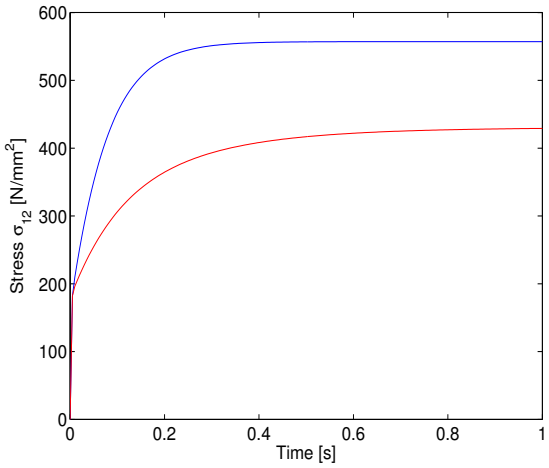

Figure 12: Maximal distance: Model 1 vs. Model 3, load 1

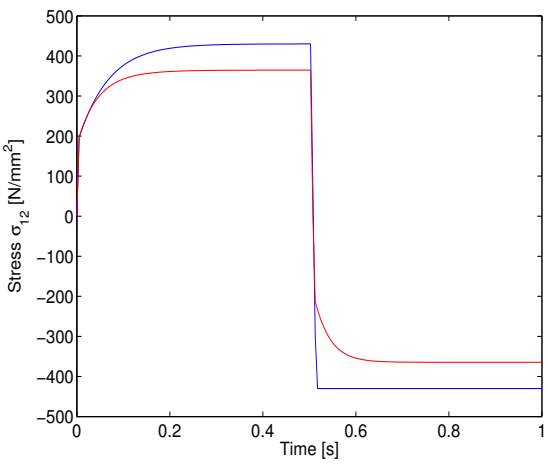

Figure 13: Maximal distance: Model 1 vs. Model 3, load 2

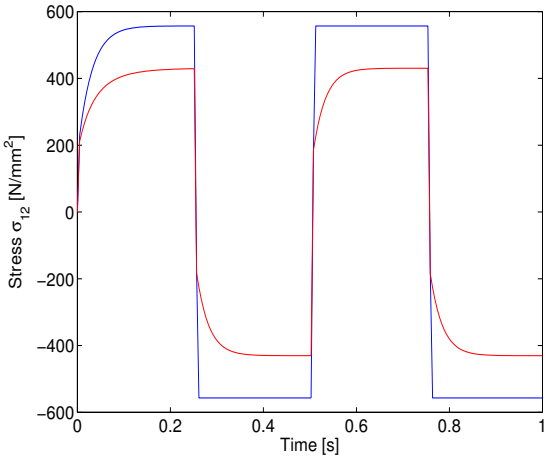

Figure 14: Maximal distance: Model 1 vs. Model 3, load 3

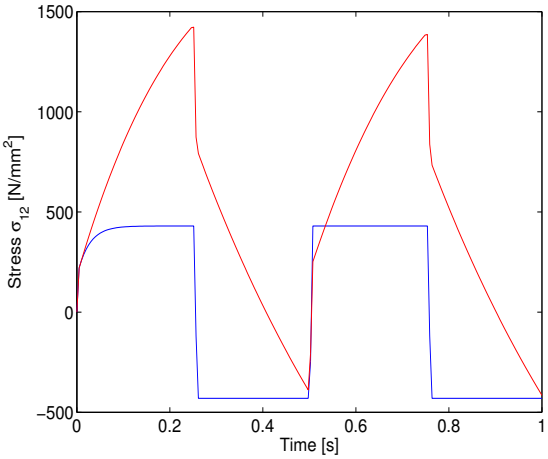

Figure 15: Maximal distance: Model 1 vs. Model 3, load 4

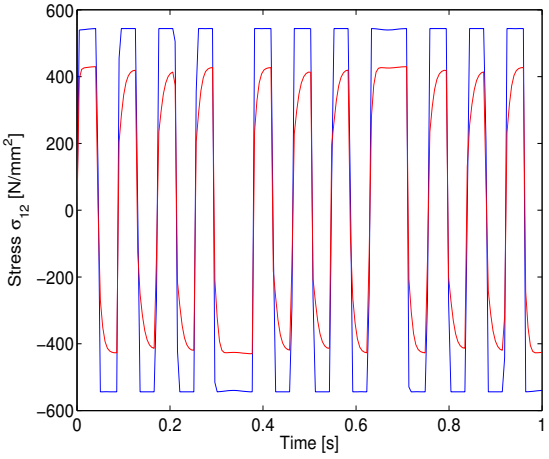

Figure 16: Maximal distance: Model 1 vs. Model 3, load 5

optimization algorithm has managed to select the parameters for Model 3 in such a way that isotropic hardening is dominant. Thus, the two curves in Figure 18 differ only in the moment of beginning of the plastic deformation in the compressive region (i.e. Bauschinger effect). Similar results are obtained also for loads 3, 4 and 5 (see Figures 19, 20 and 21).

4.3.3 Model 2 vs. Model 3

The maximal differences between Models 2 and 3 are illustrated in Figures 22 to 26. Herein, the results of Model 2 are shown in blue whereas the results of Model 3 are depicted in red. As a maximal distance for load 1, the optimization has predicted the responses in Figure 22. Here, the kinematic hardening result reaches fast saturation, whereas a steep hardening curve is predicted by Model 3. Similarly to Figure 15, the result of Model 3 for the external load 4 (Figure 25) is again characterized by a high slope of the hardening curve and, correspondingly, high stress values.

Finally, the minimal distances between the models for kinematic and combined hardening are shown in Figures 27 to 30. The monotonic test (Figure 27) again performs poorly, the responses of the two models being almost identical. Figure 29 (load 3) illustrates that the parameters of Models 2 and 3 can be set such that two very similar model curves could be obtained. Obviously, the kinematic component in Model 3 is dominating and the results are virtually identical. It seems that more cycles need to be performed (Figure 31), so that the minimal distance becomes significant. Clearly, the higher the number of cycles, the greater the cyclic hardening (increase of the stress level after each cycle) computed by Model 3, and so, finally, the larger the deviation in the model responses.

4.4 Visualization of model distances and model sensitivities

We assume for now no observation or measurement errors. For the given models $i = 1, \ldots, 3$ and the different loads f_ℓ for $\ell = 1, \ldots, 5$ we present results on the first step of the model identification algorithm. This is an off-line process and we compute the model distances γ_{ij} and the sensitivities ν_{ij}. To this end we solve the minimization problems given by equations (7) and (8), respectively. To be more precise we introduce the quantities

$$\begin{aligned} \gamma_{ij}^{\ell} &:= \min_{\theta_i, \theta_j \in \Theta} \|y_i(\theta_i, f_\ell) - y_j(\theta_j, f_\ell)\|, \\ \nu_{ij}^{\ell} &:= 2 \max_{\theta_i, \theta_j \in \Theta} \max\{\|\frac{\partial}{\partial f} y_i(\theta_i, f_\ell)\|, \|\frac{\partial}{\partial f} y_j(\theta_j, f_\ell)\|\} \end{aligned}$$

for $\ell = 1, \ldots, 5$ and $i, j = 1, \ldots, 3$, and clearly obtain

$$\gamma_{ij} = \max_{\ell=1,\ldots,5} \gamma_{ij}^{\ell} \text{ and } \nu_{ij} = \max_{\ell=1,\ldots,5} \nu_{ij}^{\ell}.$$

Later on only the values ν_{ij} and γ_{ij} will be used and are shown in Table 2 and Table 3, respectively. For the sake of presentation we show all the values $(\nu_{ij}^{\ell}, \gamma_{ij}^{\ell})$ for all models and loads in Figure 32. The loads corresponding to the maximal value are in the top right part of that plot. This allows to identify f_{ij} in equation (7b) which will be used to obtain the results of the experiments in equation (9). From the results we observe that $f_{12} = f_{13} = f_{23}$ correspond to load 5. We also observe that the load 1 is infeasible to distinguish between all models.

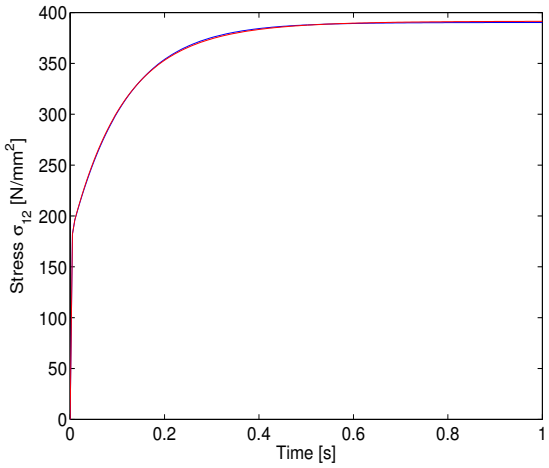

Figure 17: Minimal distance: Model 1 vs. Model 3, load 1

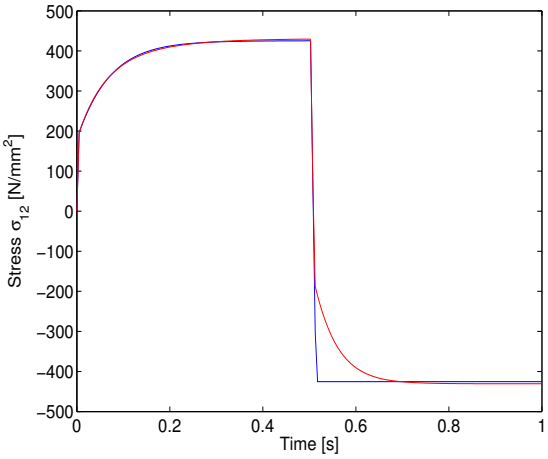

Figure 18: Minimal distance: Model 1 vs. Model 3, load 2

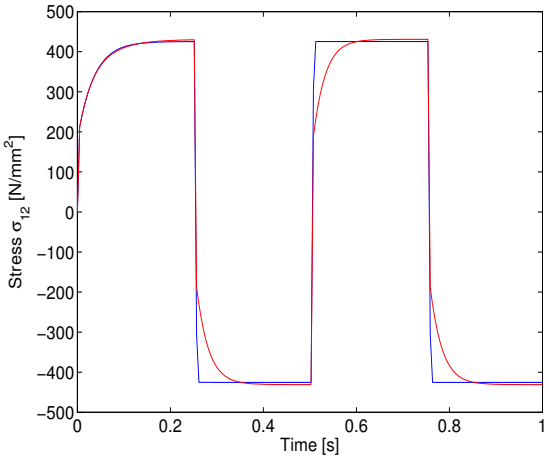

Figure 19: Minimal distance: Model 1 vs. Model 3, load 3

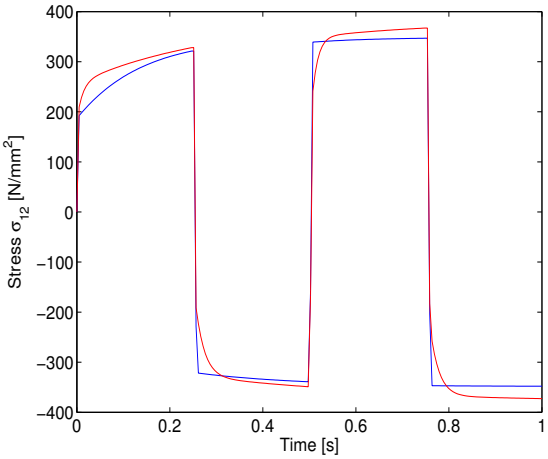

Figure 20: Minimal distance: Model 1 vs. Model 3, load 4

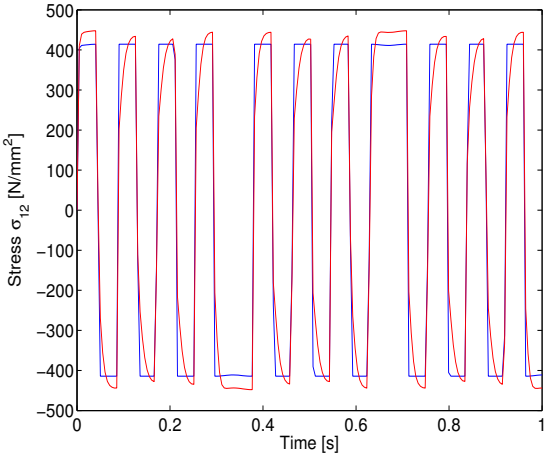

Figure 21: Minimal distance: Model 1 vs. Model 3, load 5

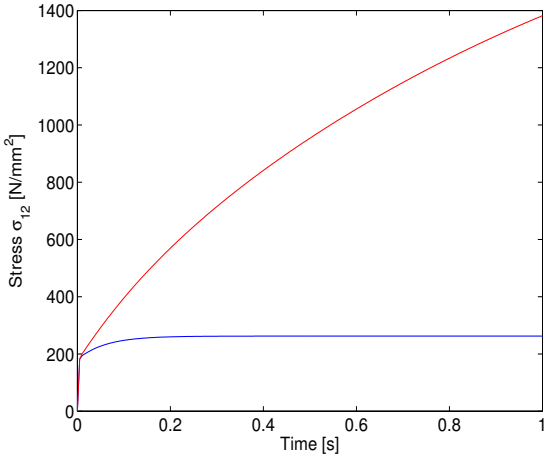

Figure 22: Maximal distance: Model 2 vs. Model 3, load 1

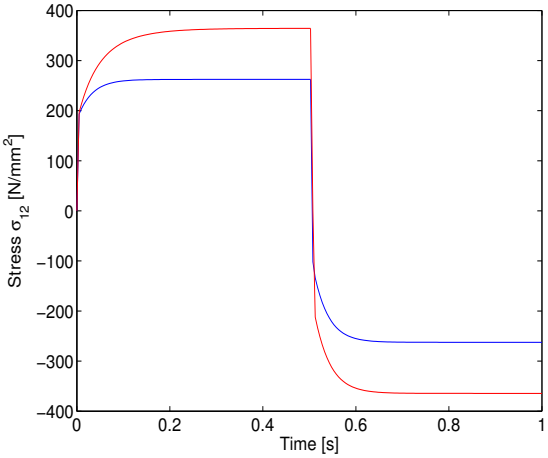

Figure 23: Maximal distance: Model 2 vs. Model 3, load 2

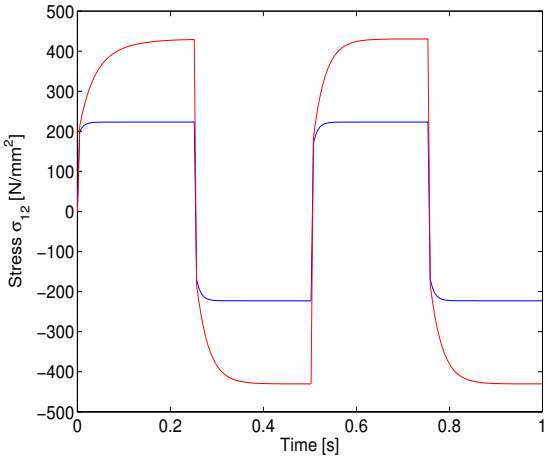

Figure 24: Maximal distance: Model 2 vs. Model 3, load 3

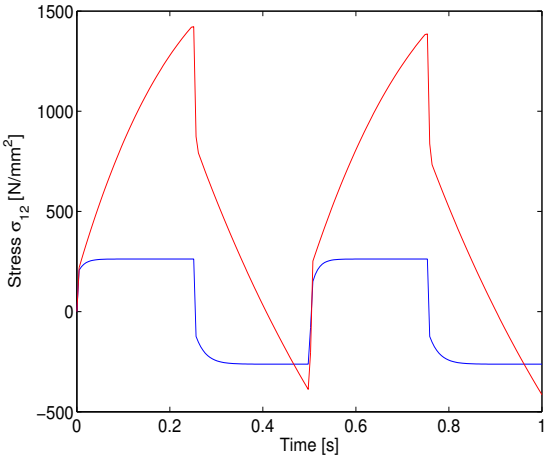

Figure 25: Maximal distance: Model 2 vs. Model 3, load 4

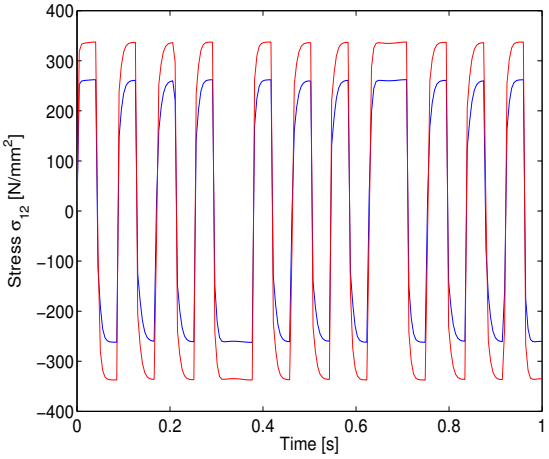

Figure 26: Maximal distance: Model 2 vs. Model 3, load 5

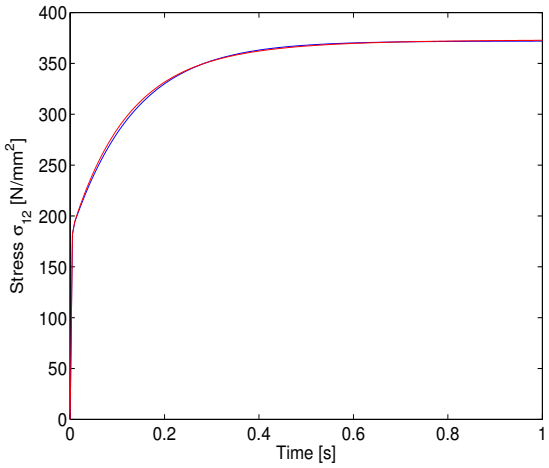

Figure 27: Minimal distance: Model 2 vs. Model 3, load 1

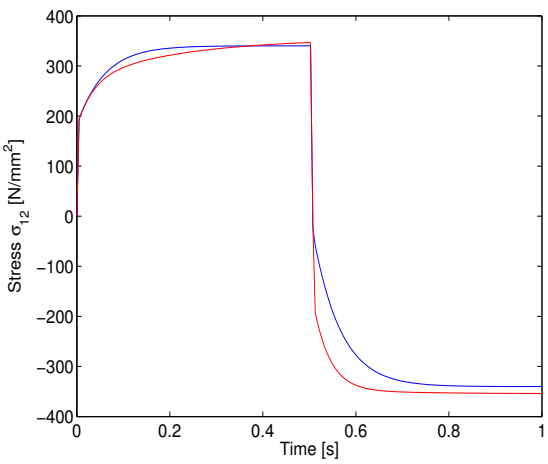

Figure 28: Minimal distance: Model 2 vs. Model 3, load 2

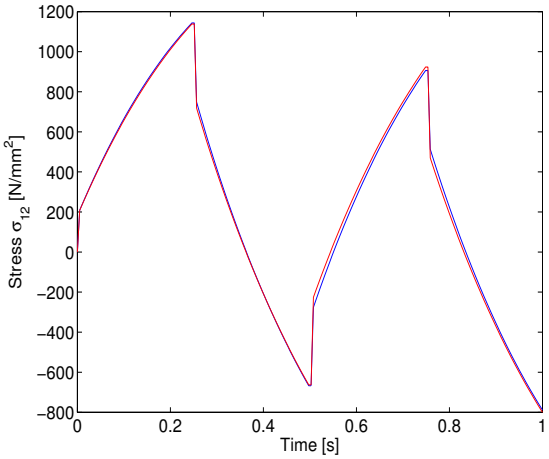

Figure 29: Minimal distance: Model 2 vs. Model 3, load 3

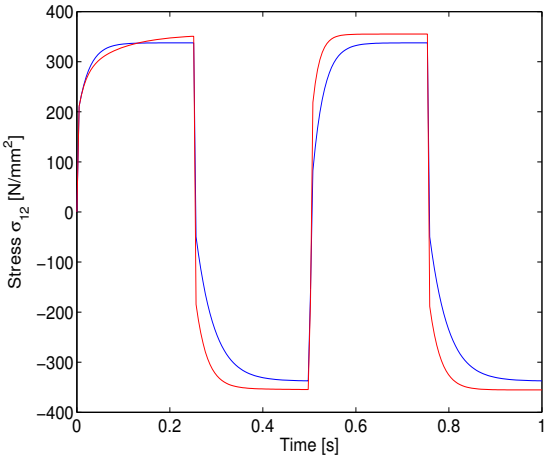

Figure 30: Minimal distance: Model 2 vs. Model 3, load 4

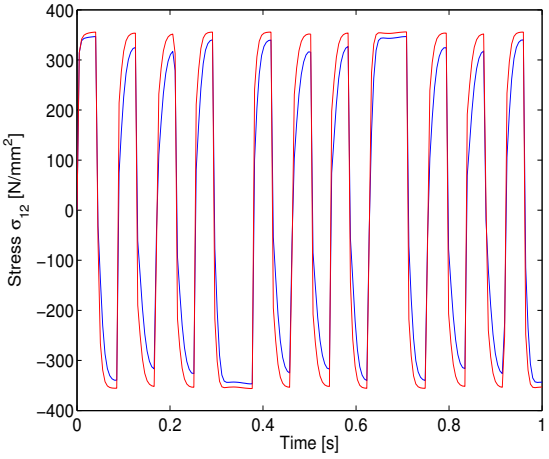

Figure 31: Minimal distance: Model 2 vs. Model 3, load 5

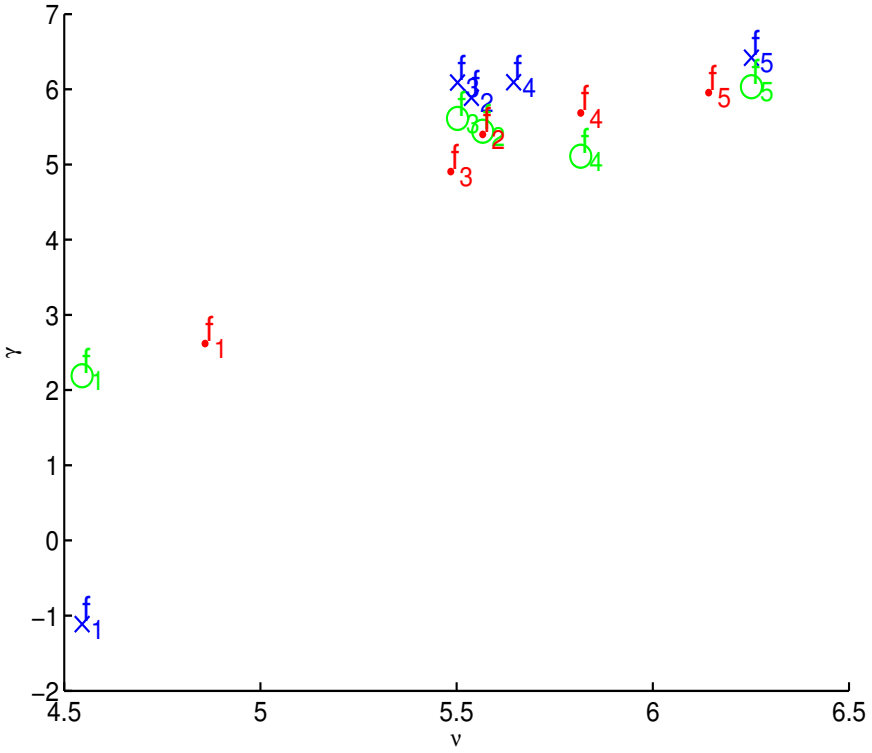

Figure 32: Graphical representation of the values $(\nu_{ij}^{\ell}, \gamma_{ij}^{\ell})$ in log-log–scale for the comparison of models (i, j) with blue crosses for $(1, 2)$, green circles for $(1, 3)$ and red dots for $(2, 3)$. The index ℓ corresponds to the applied load f_ℓ.

ν_{ij}

	1'785'100	1'785'100
1'785'100		1'388'391
1'785'100	1'388'391	

Table 2: Optimal values ν_{ij} for the models of finite strain plasticity with isotropic, kinematic and combined hardening. The values are obtained by solving the optimization problems (8).

4.5 Model identification without error in loads and observation

We use the previously determined loads and Table 3 to identify the correct model according to Theorem 2.1. In order to test our method we do not conduct experiments but set model $i = 3$ to be the correct model with a set of parameters given as $\theta = (8; 215; 12.5; 2600)$. We assume no observation error and no error on the load i.e. $\delta_{ij}^{o} = 0$, $\delta_{ij}^{f} = 0$.

In order to fulfil condition (14) we need to solve the minimization problem (11). The corresponding values are given in Table 4. We observe that the third row is zero up to machine precision and that in the third column of the table the values are larger than the corresponding values in Table 3. Furthermore, this is the only selection of columns and rows where this assertion is true and hence condition (13) holds with $l = 3$.

γ_{ij}

	2'575'318	1'002'429
2'575'318		895'033
1'002'429	895'033	

Table 3: Optimal values γ_{ij} for the models of finite strain plasticity with isotropic, kinematic and combined hardening. The values are obtained by solving the optimization problems (7).

μ_{ij}

	1'061'761	1'061'761
2'064'875		2'064'875
5.36e-10	5.36e-10	

Table 4: Optimal values μ_{ij} for the models of finite strain plasticity with isotropic, kinematic and combined hardening. The values are obtained by solving the optimization problems (11).

4.6 Determination of admissible error margins

The conditions (12) and (14) can be used to determine the range of possible observation δ^o_{ij} and measurement errors δ^f_{ij}. Equations (14) and (12) give as sufficient condition to identify the true model

$$\gamma_{ij} > 2\nu_{ij}\|\delta^f_{ij}\|_{\mathcal{F}} + 2\|\delta^o_{ij}\|_{\mathcal{Z}}.$$

In Figure 33 we depict the graphs

$$\|\delta^f_{ij}\|_{\mathcal{F}} = \frac{\gamma_{ij}}{2\nu_{ij}} - \frac{\|\delta^o_{ij}\|_{\mathcal{Z}}}{\nu_{ij}}$$

for all model combinations (i, j). The area below the graph is the range of admissible observation and measurement errors such that the true model can still be identified. We observe that the range for the norm of the error in the loads is smaller compared to the possible norm of the error in the observation. We also observe that the possible errors to differentiate between models $(1, 2)$ and $(1, 3)$ differ by the order of two magnitudes.

4.7 Model identification under errors in loads and observation

We consider now the case of pointwise uniformly distributed noise in loads and observations. The errors are bounded by $\|\delta^o_{ij}\|$ and $\|\delta^f_{ij}\|$, respectively.

Again, let $i = 3$ be the correct model with a set of parameters $\theta = (8; 215; 12.5; 2600)$. The noise on load and observation do not change the values in Table 3 and they do not have to be recomputed. However, we need to recompute the values μ_{ij} in order to fulfil condition (14).

In order to test the previously given error margins we set up two tests under measurement errors. We expect the following behavior. Perturbations of the external load corresponding to the first test case still allow to correctly identify the model. The perturbation has been chosen inside the admissible region of Figure 33. However, perturbations outside the tolerance margin depicted in Figure 33 are too large to

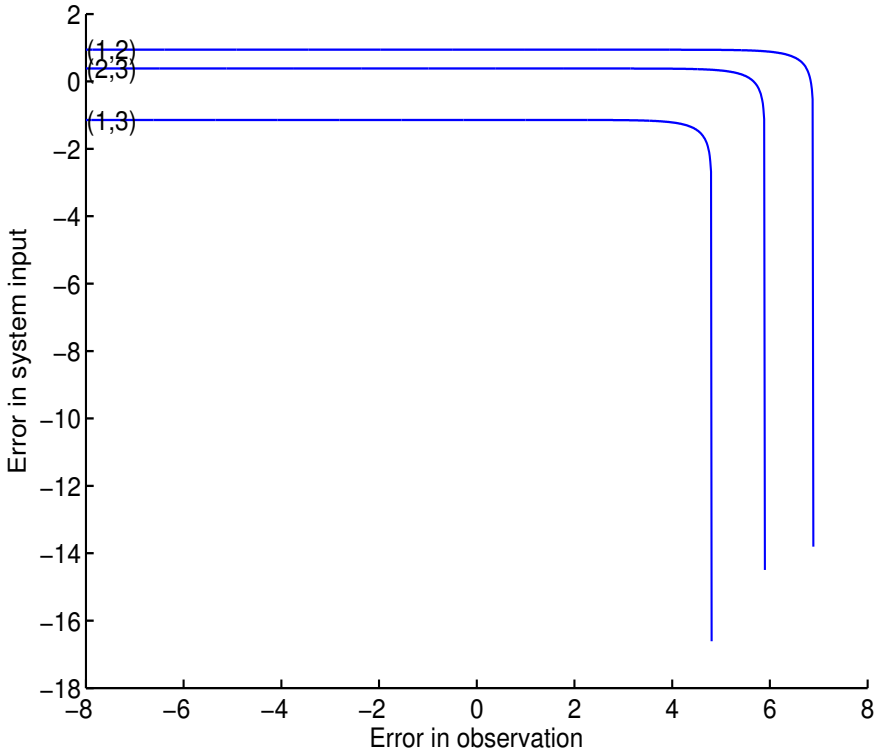

Figure 33: Possible ranges for the norm of the observation error $\|\delta^o_{ij}\|_{\mathcal{Z}}$ and measurement errors $\|\delta^f_{ij}\|_{\mathcal{F}}$ for the different models (i, j) in log-log–scale. The area enclosed by the lines is the range for the admissible errors.

uniquely identify the correct model. The expectations are confirmed by the numerical simulation. In the first case the corresponding values are given in Table 5 whereas for the second case the values are given in Table 6.

	μ_{ij}	
	1’061’761	1’061’761
2’064’875		2’064’875
4.93e-10	4.93e-10	

Table 5: Optimal values μ_{ij} for the models of finite strain plasticity with isotropic, kinematic and combined hardening. The values are obtained by solving the optimization problems (11).

	μ_{ij}	
	1’404’513	1’257’606
5’946’644		4’090’822
38’665	35’402	

Table 6: Optimal values μ_{ij} for the models of finite strain plasticity with isotropic, kinematic and combined hardening. The values are obtained by solving the optimization problems (11).

For perturbations outside the tolerance the corresponding values of μ_{ij} are given in Table 6. We observe that the third row is non–zero and larger than the applied error. Hence, the criterion (13) of Theorem 2.1 is not fulfilled and it is not possible to identify the correct model anymore.

5 Summary

We introduce a new method for model identification problems and present an application to constitutive models in metal plasticity. The sequential approach uses an off-line stage at which optimal loads are determined. These are later used to identify the previously unknown model and its parameters. Bounds on measurement errors for the observation as well as bounds for possible errors in the load are considered and criteria are provided such that the correct model still can be identified. Numerical results for model identification and several competing constitutive models are presented.

Acknowledgements. This work has been supported by DFG HE5386/8-1, the cluster of excellence EXC128 funded by the DFG and ERS Seedfunds, 2012.